



Accelerating lithium storage capability of cobalt sulfide encapsulated within anion dual-doped mesoporous carbon nanofibers

Dong-Yo Shin^a, Hyun-Gi Jo^b, Hyo-Jin Ahn^{a,b,*}

^a Program of Materials Science & Engineering, Convergence Institute of Biomedical Engineering and Biomaterials, Seoul National University of Science and Technology, Seoul 01811, Republic of Korea

^b Department of Materials Science and Engineering, Seoul National University of Science and Technology, Seoul 01811, Republic of Korea

ARTICLE INFO

Keywords:

Ultrafast lithium storage
Cobalt sulfate
Anion doping
Anode
Mesoporous carbon nanofiber

ABSTRACT

Metal sulfide materials are promising for the anodes of ultrafast lithium ion batteries (LIBs) for many potential high-technology devices because of their high electrical conductivity, high theoretical capacity, and chemical/electrochemical stability resulting from their unique crystal structures. Despite their significant advantages, these materials face an important challenge related to structural degradation, owing to the significant volume expansion of metal sulfide under ultrafast cycling conditions. This phenomenon leads to rapid capacity fading and must be improved for the practical application of ultrafast LIBs. In the present study, a unique architecture of cobalt sulfide encapsulated within anion dual (nitrogen and sulfur)-doped mesoporous carbon nanofibers (referred to as CoS-NS-PCNF) was fabricated via electrospinning and carbonization. The CoS-NS-PCNF exhibited superb ultrafast cycling performance including outstanding cycling stability (748.6 mAh g⁻¹ with capacity retention of 96.5% at 100 mA g⁻¹ after 100 cycles), a superb ultrafast cycling capacity (550.1 mAh g⁻¹ at 2000 mA g⁻¹), and excellent ultrafast cycling stability (514.6 mAh g⁻¹ with capacity retention of 93.5% at 2000 mA g⁻¹ after 500 cycles). Thus, the novel architecture has significant advantages for ultrafast lithium storage kinetics including a short lithium-ion diffusion length, a high ion/electron transfer rate, and effective prevention of volume expansion.

1. Introduction

With the continuous development of advanced electrical devices such as electric vehicles, unmanned drones, and human-body-assisted robot suits, users of electrical devices are demanding the development of higher-quality energy sources compared with those used in previous energy storage devices [1,2]. Lithium-ion batteries (LIBs) have been used in electrical devices because of their significant advantages, such as their superb energy density, long life time, low self-discharge, and eco-friendliness [3]. Despite these advantages, LIBs have been unable to satisfy the requirements (including a long operation time and short charge time) to expand the demand for high-technology devices. In particular, with the widespread use of electric vehicles around the world, interest in the characteristics of LIBs, e.g., driving distances of > 300 miles and charging times of < 10 min, is rapidly increasing [4,5]. However, owing to the energy storage limitations of anode materials such as graphite, which is commonly used in LIBs, these requirements have not yet been satisfied. In addition, the specific capacity and charging rate of LIBs are generally limited by the poor

electrochemical properties of the graphite anode material, which has a low theoretical capacity (372 mAh g⁻¹) and a low lithium diffusion rate [6].

Thus, various metal-oxide-based materials (Co₃O₄, SnO₂, and Fe₂O₃) [7–10] and metal-sulfide-based materials (FeS, NiS, and CoS) [11–14] have been extensively studied as anode materials to overcome the limitations of graphite. Compared with metal-oxide materials, metal-sulfide-based materials generally have higher electrical conductivity and higher mechanical, thermal, and chemical stability owing to their unique metal-sulfur bonding structure. Among the metal-sulfide-based materials, cobalt sulfides (CoS, CoS₂, Co₉S₈, Co₃S₄, and CoS_x) have outstanding physical, chemical, electrical, and electrochemical properties as anode materials and a higher theoretical capacity (~500–900 mAh g⁻¹) than commercial graphite [15,16]. Because of these advantages, cobalt sulfides have been used in various fields, e.g., supercapacitors, redox flow batteries, and sodium-ion batteries; however, they have limitations with regard to the nanomaterial design and complex synthesis methods. In addition, cobalt sulfides are accompanied by large volume expansion, leading to a low cycling

* Corresponding author at: Department of Materials Science and Engineering, Seoul National University of Science and Technology, Seoul 01811, Republic of Korea
E-mail addresses: sdy@seoultech.ac.kr (D.-Y. Shin), hgjo@seoultech.ac.kr (H.-G. Jo), hjahn@seoultech.ac.kr (H.-J. Ahn).

stability, poor rate capability, and large irreversible capacity, which makes them difficult to apply to anode materials in LIBs [17,18].

Thus, combining cobalt sulfide with carbon materials (graphene, carbon nanotubes, and carbon nanofibers) is effective for enhancing the structural stability by suppressing the volume expansion. Although various methods for incorporating cobalt sulfide into carbon materials have been investigated, the cobalt-sulfide-incorporated carbon materials exhibited a low rate capability and ultrafast cycling performance because the carbon materials increased the diffusion length of Li ions inserted into the cobalt sulfide.

Herein, to effectively design the nanoencapsulation structure of CoS and to achieve a high rate capability with ultrafast lithium storage kinetics, we fabricated a novel architecture comprising a mesoporous structure with a minimized lithium diffusion length and anion (N and S) dual-doped carbon nanofibers with a maximized ion/electron transfer rate as an anode material via a one-pot synthesis of electrospinning. Nanoencapsulation and a mesoporous architecture with N and S doping were formed via the decomposition of cysteine polymer and the evaporation of ZnO nanoparticles during the carbonization process. This type of mesoporous structure with anion doping had synergistic effects, enhancing the electrochemical performance, which is useful for ultrafast LIBs.

In the anion dual-doped mesoporous structure, the well-dispersed CoS nanoparticles provide a high specific capacity owing to the large number of active sites, which are insertion/desertion sites for Li ions. In addition, the volume expansion of CoS nanoparticles was significantly suppressed by the encapsulated CoS nanoparticles in the CNF, which acted as a physical buffer layer. Furthermore, the mesoporous structure with doped N and S atoms in the porous carbon nanofibers significantly reduced the Li-ion diffusion length and accelerated the ion/electron transfer rate, improving the ultrafast cycling performance. As expected, this novel architecture exhibited an outstanding ultrafast cycling capacity and excellent cycling stability when applied as the anode material of ultrafast LIBs.

2. Experiments

2.1. Chemicals

Cobalt sulfide (CoS₂, 99.98%), cobalt phthalocyanine (C₃₂H₁₆CoN, 97%), L-cysteine (C₃H₇NO₂S, 97%), zinc oxide (ZnO, < 50 nm particle size), polyacrylonitrile (PAN, Mw = 1,300,000), and N,N-dimethylformamide (DMF, 99.8%) were purchased from Sigma-Aldrich. All chemicals were used without further purification.

2.2. Synthesis of anion dual-doped mesoporous carbon nanofibers with CoS nanoparticles

Dual-doped (N and S) mesoporous carbon nanofibers (PCNFs) with CoS nanoparticles were synthesized via electrospinning and carbonization. First, 3 wt% C₃₂H₁₆CoN, 3 wt% L-cysteine, and 10 wt% PAN were dissolved in DMF followed by stirred for 5 h. Then, to form mesopores on carbon nanofibers (CNFs), 15 wt% ZnO nanoparticles were added to the prepared solution. Subsequently, the precursor solution was added to a syringe fitted with a 23-gauge needle. For the electrospinning process, the humidity in the chamber was maintained below 10%. The feeding rate of the syringe pump and DC voltage of the power supply were applied at 0.05 ml h⁻¹ and 15 kV, respectively. The distance between the aluminum collector and the needle was fixed at 15 cm during the electrospinning process. The as-spun nanofibers were stabilized at 280 °C for 2 h in air and carbonized at 800 °C for 2 h in a N₂ atmosphere (99.999%). To remove residual ZnO nanoparticles from the carbonized sample, etching was performed in a 1 M HCl solution for 3 h. After the etching process, the sample was washed several times with DI-water and dried at 80 °C for 12 h. The resulting material is hereinafter referred to as CoS-NS-PCNF. To examine the effects of the N

and S doping and the mesopores on the CNF, commercial CoS₂, commercial CoS₂-embedded CNF (CoS₂-CNF), and CoS-encapsulated N- and S-doped CNFs without ZnO nanoparticles (CoS-NS-CNF) were prepared.

2.3. Characterization

The crystal structures and chemical bonding states were analyzed using X-ray diffraction (XRD) with Cu Kα radiation in the 2θ range of 10° to 90° and X-ray photoelectron spectroscopy (XPS) with Al Kα as the X-ray source. The morphology and structure were examined via field-emission scanning electron microscopy (FESEM) and transmission electron microscopy (TEM). To analyze the elements in the samples, energy-dispersive X-ray spectroscopy (EDS) mapping was performed. The specific surface area, total pore volume, and pore-size distribution were determined via Brunauer–Emmett–Teller (BET) and Barrett–Joyner–Halenda (BJH) analyses using N₂ adsorption at 25 °C. The content of CoS in CNF was investigated using thermogravimetric analysis (TGA) from 25 °C to 800 °C in air.

2.4. Electrochemical characterization

The electrochemical performances was analyzed using coin-type cells (CR2032, Hohsen Corporation) comprising a sample (commercial CoS₂, CoS₂-CNF, CoS-NS-CNF, or CoS-NS-PCNF), a porous polypropylene membrane (Celgrad 2400) as a separator, and lithium metal foil (Honjo Chemical, 99.999%) as the cathode, and a 1.2 M LiPF₆ solution in a mixture of dimethyl carbonate and ethylene carbonate (3:7) as the electrolyte. The electrodes were prepared on Cu foil (Nippon Foil, 18 μm; functioned as the current collector) with a paste slurry, which was composed of 70 wt% sample as the active material, 10 wt% Ketjen black as the conducting material, and 20 wt% polyvinylidene fluoride as the binder. The paste-slurry-coated electrodes were dried at 100 °C for 10 h, and the mass loading of the active material in the electrode was optimized to 10.2 ± 0.3 mg/cm². All electrodes were assembled in a coin-type cell in an argon-filled glove box with a humidity and oxygen content of less than 5 ppm. Charge/discharge measurements were performed using a battery cycler system (WonATech Corp., WMPG 3000) in the potential range of 0.05–3.00 V (vs. Li/Li⁺). The cycling stability was analyzed for up to 100 cycles at a current density of 100 mA g⁻¹. The C-rate performance was examined at current densities of 100, 300, 700, 1000, 1500, and 2000 mA g⁻¹. The ultrafast cycling performance was measured for up to 500 cycles at a current density of 2000 mA g⁻¹.

3. Results and discussion

Fig. 1(a) shows the XRD patterns of commercial CoS₂, CoS₂-CNF, CoS-NS-CNF, and CoS-NS-PCNF, which were used to investigate their crystalline phases and crystallinities. The characteristic diffraction peaks of commercial CoS₂ and CoS₂-CNF were observed at ~27.9°, ~32.3°, ~36.3°, ~39.8°, ~46.4°, and ~54.9°, corresponding to the (1 1 1), (2 0 0), (2 1 0), (2 1 1), (2 2 0), and (3 1 1) planes of the CoS₂ phase by fabricated commercial CoS₂ (space group of Pa3, JCPDS card no. 41–1471), respectively, without any other phases [19]. The main diffraction peaks of CoS-NS-CNF and CoS-NS-PCNF were observed at ~30.6°, ~35.3°, ~46.9°, and ~54.4°, corresponding to the (1 0 0), (1 0 1), (1 0 2), and (1 1 0) planes of the CoS phase with the space group P63/mmc (194) (JCPDS card no. 65–3418), respectively [20]. Because the ZnO nanoparticles were completely removed by the etching process, no diffraction peaks other than the CoS peaks were observed.

To investigate the chemical states of CoS-NS-PCNF, XPS was performed. The XPS spectrum of CoS-NS-PCNF composed of C 1s, N 1s, S 2p, O 1s, and Co 2p was calibrated using the C 1s binding energy (284.5 eV). The full XPS spectrum of CoS-NS-PCNF exhibited C 1s, N 1s, S 2p, O 1s, and Co 2p peaks, indicating the presence of C, N, S, O, and Co, without any another impurity phases (Fig. S1). As shown in

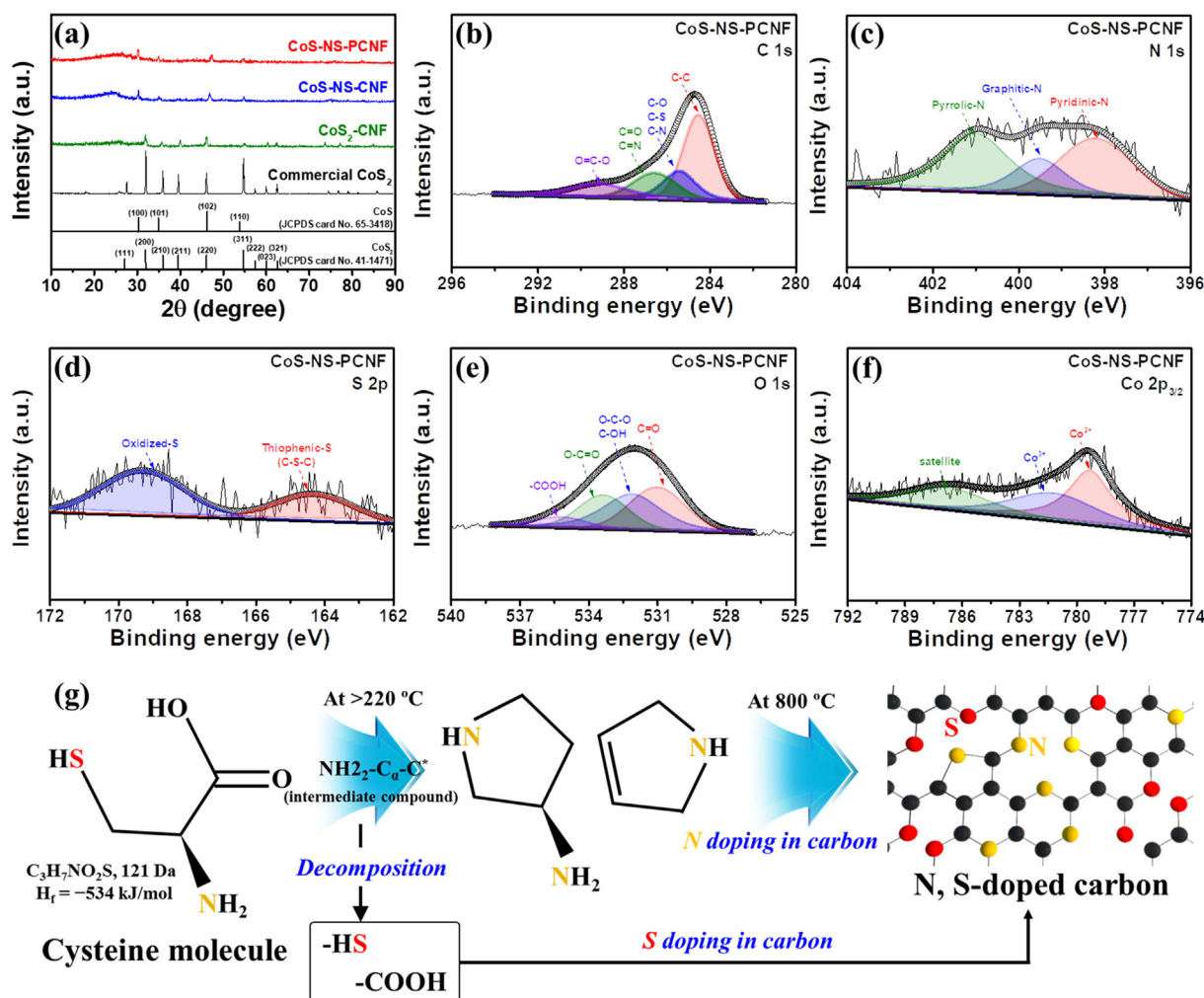


Fig. 1. (a) XRD patterns of commercial CoS_2 , CoS_2 -CNF, CoS -NS-CNF, and CoS -NS-PCNF, XPS spectra obtained from (b) C 1s, (c) N 1s, (d) S 2p, (e) O 1s, (f) Co $2p_{3/2}$ of CoS -NS-PCNF, and (g) schematic illustration of N and S doping mechanism using decomposition of cysteine polymer.

Fig. 1(b), the C 1s spectrum of CoS -NS-PCNF exhibited typical signals at ~ 284.6 , ~ 285.4 , ~ 286.4 , and ~ 289.1 eV, corresponding to the C-C, C-(O, S, and N), C=(O and N), and O = C-O binding states, respectively [21]. In particular, the C-N and C-S binding states were formed by N and S sources provided by cysteine polymers [22]. The N 1s XPS spectrum of CoS -NS-PCNF (Fig. 1(c)) exhibited three signals at ~ 398.2 , ~ 399.5 , and ~ 401.0 eV, corresponding to the pyrrolic-, graphitic-, and pyridinic-N binding states, respectively (Fig. S2(a)) [23].

The N atoms combined with two C atoms located at the edges of the graphene lattice, forming a pyridinic-N structure. A pyrrolic-N structure coupled with two C atoms was generated at the graphene lattice plane, constituting a heterocyclic ring. Pyridinic-N and pyrrolic-N can increase the number of active sites of graphene by providing N2C bonds, which are related to broken C-C bonds. The graphitic-N structure is formed by replacing N atoms with carbon atoms in the graphene lattice. In addition, doped N atoms in the graphene lattice plane form one p-electron that contributes to the π -system of the carbon structure, which can improve the electrical conductivity owing to the extra electrons in the CNFs [23,24].

The S 2p spectrum of CoS -NS-PCNF (Fig. 1(d)) exhibited two signals at ~ 164.3 eV and ~ 169.3 eV, corresponding to the thiophenic-S (C-S-C) and oxidized-S (-C-SO_x-C-) binding states, respectively [25]. Thiophenic-S is formed by one S atom with two neighboring C atoms, which provides extra electrons via spin-orbit coupling. In addition, an oxidized S bond appeared, which resulted from existing S combined with O molecules at the edge of the graphene plane [25,26]. S-C bonds are

similar to N-C bonds; however, because S atoms (1.09 Å) have a larger atomic radius than C (0.91 Å), they prefer a thiophenic binding state rather than a pyrrolic-N binding state (Fig. S2(b)) [27]. The lattice distance of graphite (3.40 Å) can be increased to 3.73 Å by the thiophenic-S binding state, which contributes to fast ion intercalation into graphite [28].

The O 1s spectrum of CoS -NS-PCNF (Fig. 1(e)) exhibited four signals at ~ 530.9 , ~ 532.1 , ~ 533.2 , and ~ 535.1 eV, corresponding to the C=O, O-C-O or C-OH, O-C=O, and -COOH bonds, respectively [29]. The O-containing bonds in the CNFs were generated on the surface by the oxidation of C and absorption of O molecules. As shown in Fig. 1(f), the Co $2p_{3/2}$ spectrum exhibited three types of Co(II), Co(III), and satellite peaks at binding energies of ~ 779.2 , ~ 781.1 , and ~ 786.8 eV, respectively, confirming the presence of the CoS phase. The crystal structure of CoS was composed of two Co^{2+} and two S^{2-} in the unit cell (Fig. S2(c)) [30]. Co^{2+} is coordinated with six S^{2-} ions, which form the CoS_6 octahedron sharing face and edge, each other [31]. In particular, CoS has numerous redox reaction sites and excellent electrical properties owing to its crystal structure. Fig. 1(g) shows the cysteine decomposition and N and S doping processes during the stabilization and carbonization. The cysteine polymer had a $C_3H_7NO_2S$ molecular structure with chemical properties of 121 Da (unified atomic mass unit) and $H_f = -534$ kJ mol⁻¹ (latent heat of melting). The decomposition equation for cysteine is as follows [22,32]:



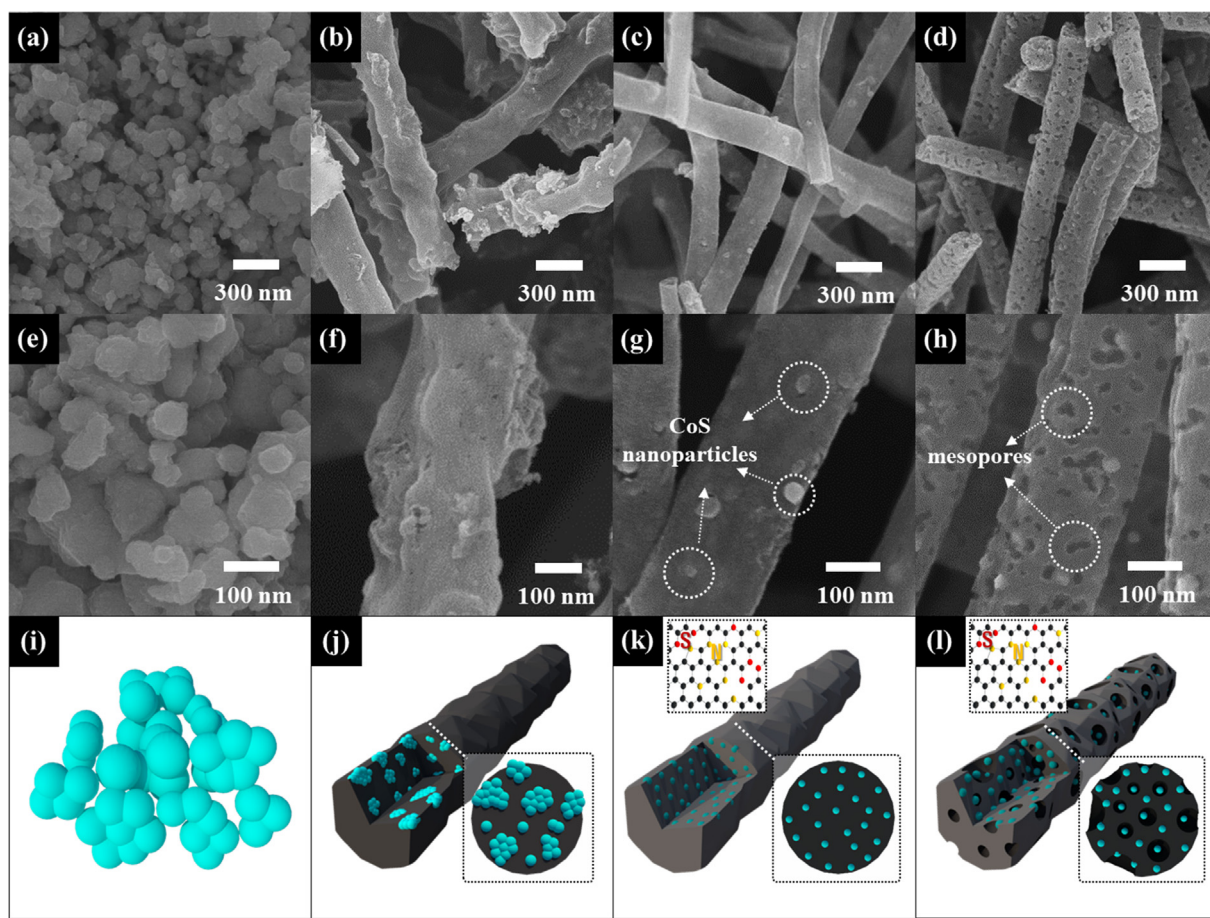


Fig. 2. (a–d) Low and (e–h) high-magnification FESEM images, and (i–l) schematic illustration of commercial CoS_2 , CoS_2 -CNF, CoS-NS-CNF , and CoS-NS-PCNF .

Initially, as the temperature increases, the CO_2 molecules decompose, and then the $-\text{C}^*\text{OOH}$ and $-\text{SH}$ groups start to decompose at $> 220^\circ\text{C}$. At this time, the decomposed $-\text{SH}$ molecules remain in the CNFs as an S-doping source. The intermediate compound $\text{NH}_2-\text{C}_\alpha-\text{C}^*$ formed during the decomposition generates 3-pyrrolidinamine and 2,5-Dihydro-1H-pyrrole ($\text{C}_4\text{H}_7\text{N}$). Finally, the remaining S in the $-\text{SH}$ molecule and N in the $\text{C}_4\text{H}_7\text{N}$ molecule are doped into CNFs during the carbonization process (at 800°C). Thus, dual-doped anions with uniform N and S dopants can be synthesized using the cysteine polymer [22,32].

Fig. 2 shows (a)–(d) low magnification, (e)–(h) high-magnification FESEM images, and (i)–(l) schematics of the commercial CoS_2 , CoS_2 -CNF, CoS-NS-CNF , and CoS-NS-PCNF , respectively. The commercial CoS_2 had a size of ca. 74.8–123.6 nm, with a spherical shape (Fig. 2(a), 2(e), and 2(i)). In contrast, CoS_2 -CNF, CoS-NS-CNF , and CoS-NS-PCNF had diameters of ~ 255.9 – 308.8 nm, ~ 198.5 – 238.6 nm, and ~ 184.0 – 229.1 nm, respectively, and exhibited interconnected network structures that facilitated efficient charge transfer, e.g., ions and electrons during cycling (Fig. 2(b)–(d)) [18]. Furthermore, the CoS-NS-CNF and CoS-NS-PCNF exhibited well-dispersed CoS nanoparticles in the CNFs compared with the CoS_2 -CNF without the cysteine polymer.

In general, although CoS nanoparticles are easily aggregated owing to their unstable state with a high surface energy, in the cases of CoS-NS-CNF and CoS-NS-PCNF , the added cysteine polymer improved the dispersibility of the CoS nanoparticles in the carbon by reducing the surface energy of CoS [33]. While the CoS-NS-CNF exhibited a smooth surface (Fig. 2(g) and (k)), the CoS-NS-PCNF exhibited a rough surface with mesopores (Fig. 2(h) and (l)) owing to the reduction and evaporation of ZnO particles during the carbonization process (Fig. S3) [4]. During the carbonization process, ZnO particles dissolved, were

reduced to the Zn and were thermodynamically stabilized. Owing to the Kirkendall effect, ZnO particles are externally diffused and partially evaporated to form mesopores in the CNFs [34]. Furthermore, the amount of CoS in CoS_2 -CNF, CoS-NS-CNF , and CoS-NS-PCNF was identified using TGA measurement, as shown in Fig. S4. The CoS_2 -CNF, CoS-NS-CNF , and CoS-NS-PCNF exhibit weight losses of 33.5%, 33.8%, and 34.7%, implying the existence of CoS nanoparticles in CNFs. The unique mesoporous architecture of CoS-NS-PCNF , including the well-dispersed CoS nanoparticles in the PCNFs provided numerous active sites as well as a short ion diffusion length, which can improve the ultrafast cycling performance.

To further investigate the structure of CoS-NS-PCNF , transmission electron microscopy with energy-dispersive X-ray spectrometry mapping (TEM and TEM-EDS mapping, Gwangju Center, Korea Basic Science Institute) was performed (Fig. 3). The CoS-NS-PCNF showed mesopores in the PCNFs (Fig. 3(a)). In addition, the dark spots in CoS-NS-PCNF (Fig. 3(b)) exhibited well-dispersed CoS nanoparticles with sizes of ~ 9.8 – 20.4 nm inside the CNFs. Remarkably, the CoS nanoparticles were encapsulated in carbon (Fig. S5). These results indicate that a mesoporous structure with CoS nanoparticles was formed by the reduction and evaporation of ZnO particles due to the decomposition of the cysteine polymer on the CoS nanoparticles [4,34]. The cysteine polymer had a $\text{C}_3\text{H}_7\text{NO}_2\text{S}$ molecule. The C atoms form a carbon layer on the surface of CoS nanoparticles via decomposition of the $\text{C}_3\text{H}_7\text{NO}_2\text{S}$ molecule during the carbonization process in a N_2 atmosphere [32,33]. According to the EDS results (Fig. 3(c) and S6), all elements (C, N, S, and Co) were uniformly dispersed, indicating that the CoS nanoparticles and doped N and S atoms were well dispersed in the PCNFs.

To determine the specific surface area and pore types of the samples, Brunauer-Emmett-Teller (BET) measurements, which were used

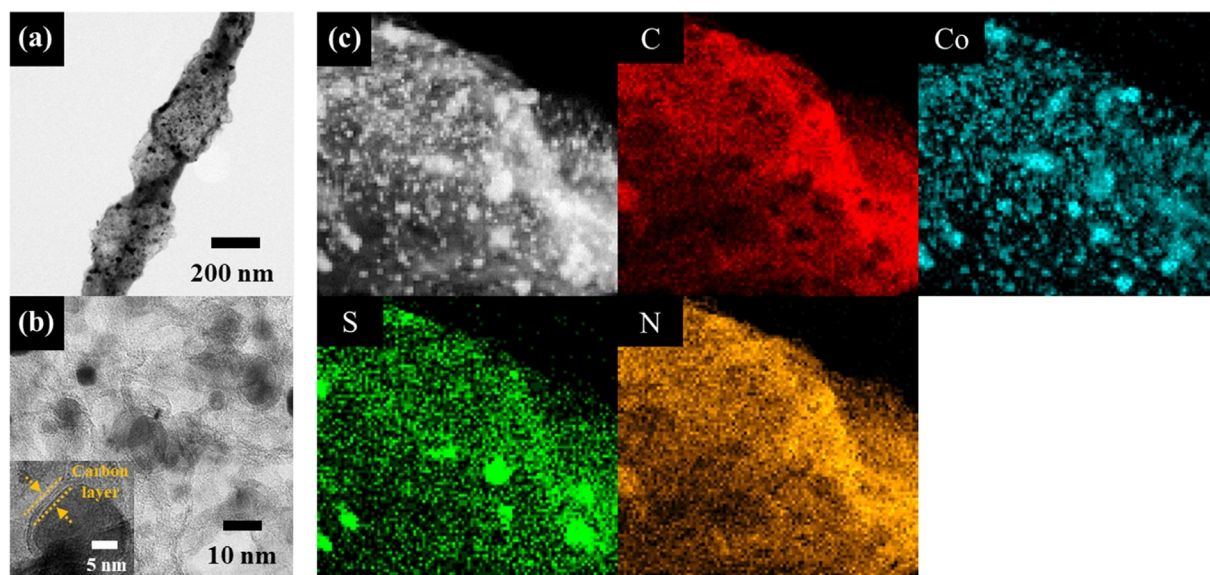


Fig. 3. (a) Low and (b) high-magnification TEM images, and (c) TEM-EDS mapping images obtained from CoS-NS-PCNF.

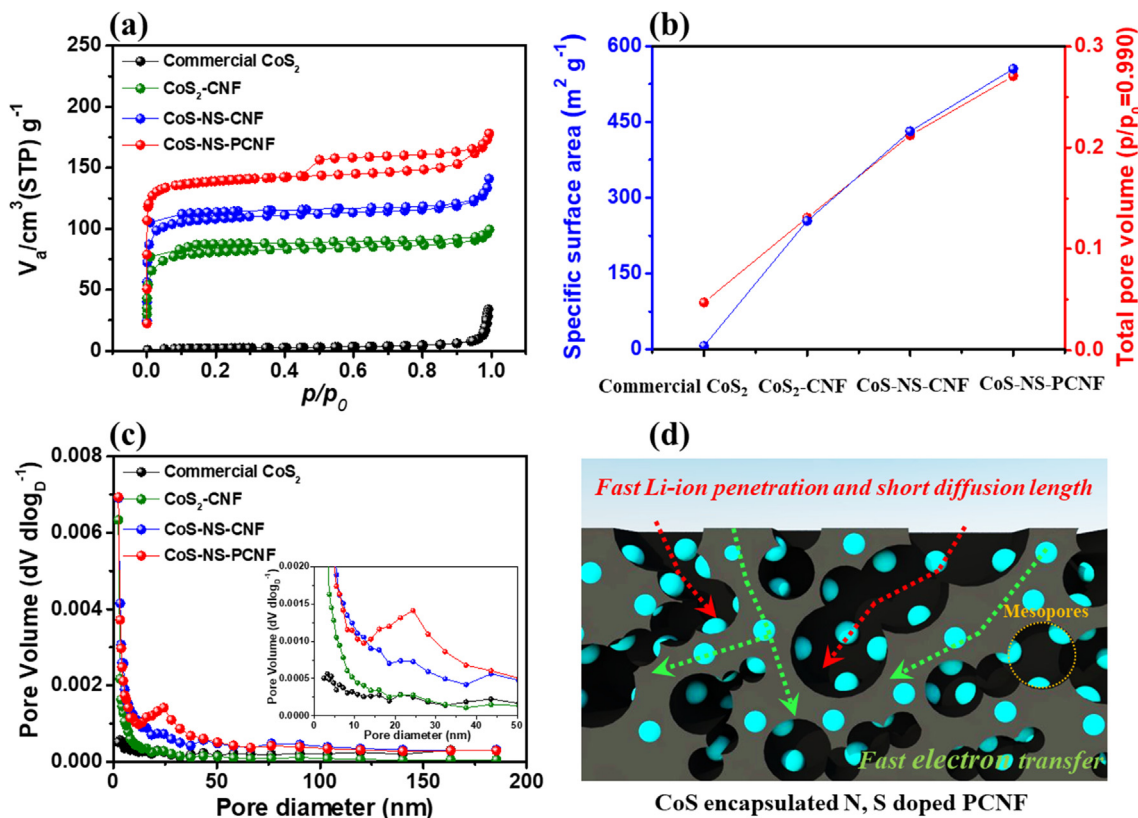


Fig. 4. (a) N_2 adsorption/desorption isotherms, (b) specific surface area and total pore volume, (c) BJH pore size distribution between 0.2 and 200 nm obtained from all samples, (d) schematic illustration of ion/electron diffusion mechanism of CoS-NS-PCNF.

by N_2 adsorption/desorption isotherms, were analyzed (Fig. 4(a)). The isotherms of commercial CoS_2 , CoS_2 -CNF, and CoS-NS-CNF exhibited type-I characteristics as defined by the International Union of Pure and Applied Chemistry. These characteristics are related to micropores with pore widths of < 2 nm on the surface [35]. However, the isotherms of CoS-NS-PCNF exhibited type-IV characteristics corresponding to mesopores with pore widths of 2–50 nm at high pressures of $P/P_0 > 0.45$ [35]. The specific surface areas and total pore volumes were $7.1 \text{ m}^2 \text{ g}^{-1}$ and $0.05 \text{ cm}^3 \text{ g}^{-1}$ for commercial CoS_2 , $254.5 \text{ m}^2 \text{ g}^{-1}$ and $0.13 \text{ cm}^3 \text{ g}^{-1}$

for CoS_2 -CNF, $421.6 \text{ m}^2 \text{ g}^{-1}$ and $0.21 \text{ cm}^3 \text{ g}^{-1}$ for CoS-NS-CNF, and $548.2 \text{ m}^2 \text{ g}^{-1}$ and $0.27 \text{ cm}^3 \text{ g}^{-1}$ for CoS-NS-PCNF (Fig. 4(b)).

The specific surface area and total pore volume of CoS-NS-PCNF were approximately 1.30 and 1.29 times larger than those of CoS-NS-CNF, respectively, owing to the mesopores formed in the CNFs. Fig. 4(c) shows the pore volumes and pore diameter distributions obtained using BJH measurements. The mesopore size of CoS-NS-PCNF was higher than that of commercial CoS_2 and CoS-NS-CNF at 15 nm to 50 nm because of the mesopores formed by the reduction and evaporation of

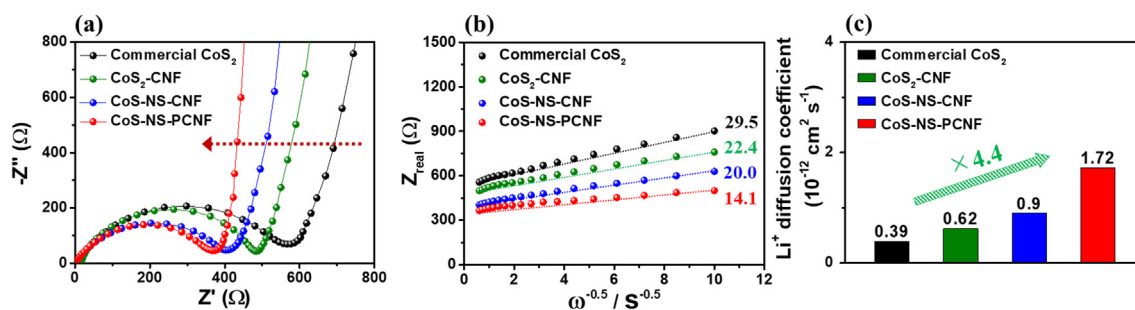


Fig. 5. (a) Nyquist plots and (b) relationship between Z_{real} and $\omega^{-1/2}$ in the low frequency range of Nyquist plots, and (c) Li ion diffusion coefficient of commercial CoS_2 , $\text{CoS}_2\text{-CNF}$, CoS-NS-CNF , and CoS-NS-PCNF .

the added ZnO nanoparticles. These results are in good agreement with the SEM and TEM results. The high specific surface area and high mesopore distribution of CoS-NS-PCNF are key factors that are well-known to reduce the Li ion diffusion length and improve the Li ion penetration [36,37]. Furthermore, doped N and S atoms with mesopores in CoS-NS-PCNF can accelerate the fast electron transfer and enhance the penetration of the electrolyte, resulting in ultrafast energy storage performance (Fig. 4(d)).

To evaluate the electrochemical kinetics of the Li ions and electrons, electrochemical impedance spectroscopy (EIS) was performed using coin-type cells comprising commercial CoS_2 , $\text{CoS}_2\text{-CNF}$, CoS-NS-CNF , and CoS-NS-PCNF . Fig. 5(a) shows Nyquist plots of all the samples at the open-circuit potential in the frequency range of 10^5 to 10^{-2} Hz. In the high-frequency region, the semicircle corresponds to the charge transfer resistance (R_{ct}) between the electrode and electrolyte. In the low-frequency region, the inclined line (referred to as the Warburg impedance) is attributed to Li ion diffusion in the electrode [38]. Among the samples, CoS-NS-PCNF had the lowest R_{ct} and Warburg impedance. The low R_{ct} is attributed to the formation of extra electrons associated with p-electrons in the π -system by N and S doping [23,25].

Owing to the electrical behavior of the samples, the electrical conductivity was $2.5 \times 10^2 \text{ S cm}^{-1}$ for commercial CoS_2 , $3.2 \times 10^2 \text{ S cm}^{-1}$ for $\text{CoS}_2\text{-CNF}$, $7.4 \times 10^2 \text{ S cm}^{-1}$ for CoS-NS-CNF , and $7.9 \times 10^2 \text{ S cm}^{-1}$ for CoS-NS-PCNF (Fig. S7). The Warburg impedance of the CoS-NS-PCNF was clearly reduced because the mesoporous structure with doped N and S atoms provided a short Li ion diffusion length and wide ion diffusion pathway (Fig. 5(b)). As shown in Fig. 5(c), the Li ion diffusion coefficients of all the electrodes were obtained from the low-frequency slopes of the EIS data using Eqs. (2) and (3) [5,38].

$$Z_{\text{real}} = R_e + R_{\text{ct}} + \sigma_w \omega^{-1/2} \quad (2)$$

$$D = R^2 T^2 / 2 A^2 n^4 F^4 C^2 \sigma_w^2 \quad (3)$$

where R_e and σ_w represent the bulk resistances corresponding to the resistance of the components (electrode, electrolyte, and separator) in the cell and the Warburg impedance coefficient corresponding to the resistance of Li ion diffusion in the material, respectively. D , A , and n represent the Li ion diffusion coefficient, electrode area, and number of electrons per molecule, respectively. R , F , and C represent the gas constant, Faraday constant, and molar concentration of Li ions, respectively. The Li ion diffusion coefficient was larger for the CoS-NS-PCNF electrode ($1.72 \times 10^{-12} \text{ cm}^2 \text{ s}^{-1}$) than for other samples ($0.39 \times 10^{-12} \text{ cm}^2 \text{ s}^{-1}$ for commercial CoS_2 , $0.62 \times 10^{-12} \text{ cm}^2 \text{ s}^{-1}$ for $\text{CoS}_2\text{-CNF}$, and $0.90 \times 10^{-12} \text{ cm}^2 \text{ s}^{-1}$ for CoS-NS-CNF). This suggests that the mesoporous structure of CoS-NS-PCNF with doped N and S atoms improved the ultrafast Li storage kinetics of LIBs owing to short lithium diffusion lengths and fast ion/electron transfer rates.

Fig. 6(a) shows the cycling stability of the charge/discharge performance measured at a low current density of 100 mA g^{-1} over 100 cycles in the voltage range of 0.05–3.0 V (vs. Li/Li^+). After the cycling stability test, the commercial CoS_2 exhibited a low specific discharge capacity of 271.2 mAh g^{-1} with capacity retention of 36.1% owing to

the excessive volume expansion, which caused rapid capacity fading [15,16]. Thus, the composition of CoS with carbon is necessary to effectively suppress volume expansion. For this reason, CoS-NS-PCNF exhibited a higher specific capacity (748.6 mAh g^{-1} with excellent capacity retention of 96.5%) than commercial CoS_2 (specific capacity of 271.2 mAh g^{-1} with a capacity retention of 34.5%), $\text{CoS}_2\text{-CNF}$ (specific capacity of 508.6 mAh g^{-1} with capacity retention of 63.6%), and CoS-NS-CNF (specific capacity of 667.6 mAh g^{-1} with capacity retention of 86.9%). This is attributed to the efficient dispersion of the CoS nanoparticles in PCNF. Furthermore, the cyclic voltammetry (CV) curves and charge–discharge curves of all samples showed typical electrochemical behavior, as shown in Figs. S8 and S9, respectively.

Fig. 6(b) shows the rate performance of the commercial CoS_2 , $\text{CoS}_2\text{-CNF}$, CoS-NS-CNF , and CoS-NS-PCNF at current densities of 100, 300, 700, 1000, 1500, and 2000 mA g^{-1} . With an increase in the current density from 100 to 2000 mA g^{-1} , while the specific capacity of commercial CoS_2 rapidly decreased, the composition of CoS with carbon exhibited an outstanding specific capacity. However, despite the combination of CoS with carbon, the $\text{CoS}_2\text{-CNF}$ exhibited low rate performance owing to the agglomerated CoS nanoparticles in the CNFs. In contrast, the CoS-NS-CNF and CoS-NS-PCNF exhibited higher specific capacities than the commercial CoS_2 and $\text{CoS}_2\text{-CNF}$ because of the well-dispersed CoS nanoparticles in the N- and S-doped carbon, which can prevent volume expansion with a high electrical conductivity. In particular, the CoS-NS-PCNF exhibited remarkable rate performance of $822.1\text{--}550.4 \text{ mAh g}^{-1}$ with current densities of 100–2000 mA g^{-1} , which was the highest among the samples (Fig. S10). Furthermore, the electrochemical performances of CNF and NS-CNF electrodes are shown in Fig. S11.

These results indicate that the enhancement of the electrochemical kinetics was primarily due to the efficient improvement of the Li ion diffusion and electron transfer caused by the mesoporous structure and anion dual doping of the PCNFs [36,37]. This result implies outstanding electrochemical performance at a high current density compared with previous reported CoS-based electrodes (Fig. 6(c)) [17,39–47]. Fig. 6(d) shows the results of ultrafast cycling stability tests of commercial CoS_2 , $\text{CoS}_2\text{-CNF}$, CoS-NS-CNF , and CoS-NS-PCNF at a high current density of 2000 mA g^{-1} over 500 cycles. Compared with the commercial CoS_2 (60.5 mAh g^{-1} after 500 cycles), $\text{CoS}_2\text{-CNF}$ (140.7 mAh g^{-1} after 500 cycles), and CoS-NS-CNF (220.2 mAh g^{-1} after 500 cycles), the CoS-NS-PCNF exhibited superb ultrafast cycling performance at a specific capacity of 514.6 mAh g^{-1} with a capacity retention of 93.5% after 500 cycles at a current density of 2000 mA g^{-1} .

Fig. 7(a) shows Nyquist plots of commercial CoS_2 and CoS-NS-PCNF obtained from fresh cells evaluated at a current density of 2000 mA g^{-1} after 500 cycles. The commercial CoS_2 exhibited a significantly increased resistance with a high Warburg impedance owing to electrode degradation caused by the volume expansion of CoS nanoparticles. Even after the ultrafast cycling test at 2000 mA g^{-1} over 500 cycles, the resistance and Warburg impedance of CoS-NS-PCNF remained low owing to the suppression of the volume expansion and the improved

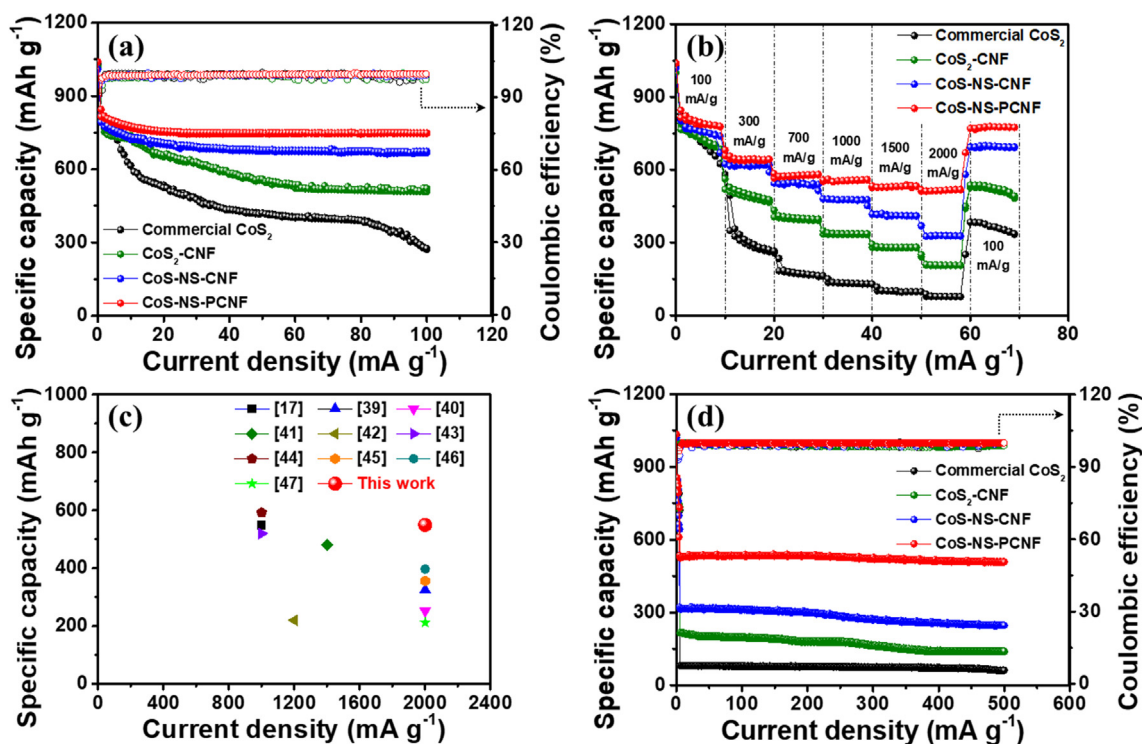


Fig. 6. (a) Cycling stability test at current density of 100 mA g^{-1} up to 100 cycles, (b) rate-performance at current densities of $100\text{--}2000 \text{ mA g}^{-1}$, (c) competition of high-rate performance with previously reported CoS-based anode materials in the LIBs, and (d) ultrafast cycling stability at current density of 2000 mA g^{-1} up to 500 cycles.

electrical conductivity. In general, CoS nanoparticles are subjected to extreme stress under ultrafast cycling conditions owing to their accelerated volume expansion [48]. Nevertheless, for CoS nanoparticles encapsulated in PCNFs, the carbon matrix suppresses the volume expansion of CoS nanoparticles. In particular, the empty spaces around the CoS nanoparticles effectively relieve the stress caused by volume expansion (Fig. 7(b)) [49,50]. In addition, after 500 cycles at current density of 2000 mA/g , the surface morphology of commercial CoS₂ is severely destructed with surface crack due to high volume expansion of commercial CoS₂ (diameter of commercial CoS₂ increased from $\sim 74.8\text{--}123.6 \text{ nm}$ to $\sim 106.4\text{--}160.2 \text{ nm}$), as shown in Fig. S12. On the other hand, the CoS-NS-PCNF electrode displayed a surface structure similar to the initial state due to increased structural stability. Although the CoS nanoparticles are slightly increased ($\sim 14\text{--}28 \text{ nm}$), their structure is still maintained with well-dispersed CoS nanoparticles, as shown in Fig. S13.

Thus, in this study, CoS-NS-PCNF with mesoporous structures and

anion dual-doping in the CNFs exhibited ultrafast cycling performance. The improvement of the ultrafast cycling performance is ascribed to three main effects (Fig. 8): (I) the high specific capacity is attributed to the well-dispersed CoS nanoparticles in the PCNFs, which provided numerous active sites (Fig. S14(a)); (II) the outstanding cycling stability is attributed to the encapsulated CoS nanoparticles in the PCNFs, which prevented and relieved the stress caused by volume expansion (Fig. S14(b)); and (III) the superb ultrafast cycling performance is ascribed to the mesopores with doped N and S atoms in the PCNFs, which provided an excellent fast electrochemical reaction between the CoS nanoparticles and Li ions owing to the reduced Li ion diffusion lengths and fast ion/electron transfer rates (Fig. S14(c)). Thus, we believe that the novel CoS-NS-PCNF electrode has great potential as an anode material for ultrafast LIBs.

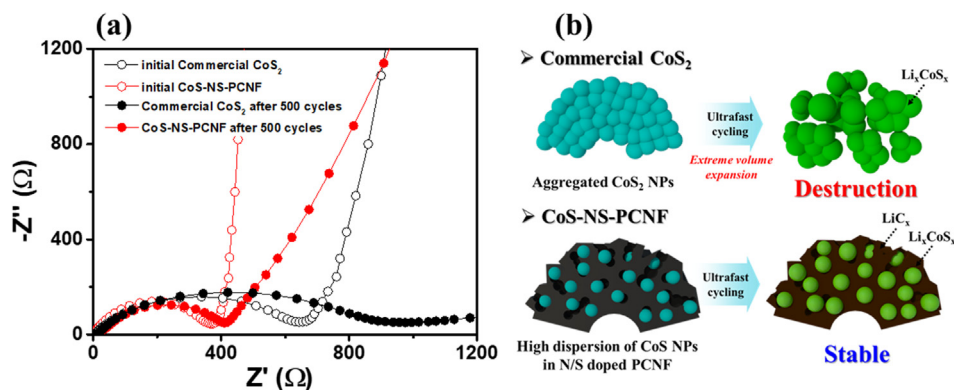


Fig. 7. (a) Comparison of Nyquist plots obtained from the initial and 500th cycle for commercial CoS₂ and CoS-NS-PCNF at current density of 2000 mA g^{-1} , (b) schematic illustration of degradation mechanism of commercial CoS₂ and CoS-NS-PCNF.

Novel architecture for ultrafast lithium storage

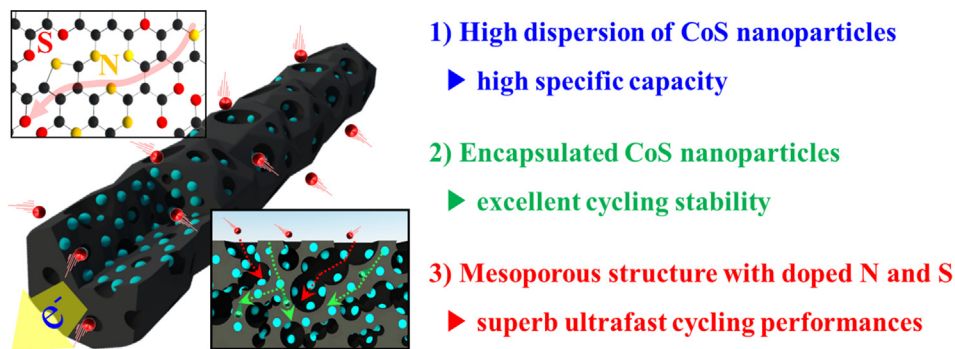


Fig. 8. Schematic illustration of the three main effects on CoS-NS-PCNF for improving ultrafast lithium storage performances. Schematic illustration of ion diffusion and electron transport in CoS-NS-PCNF with three main effects for ultrafast LIBs.

4. Conclusions

We successfully synthesized CoS nanoparticles encapsulated in anion dual-doped mesoporous carbon nanofibers (CoS-NS-PCNF) as an anode material via electrospinning and carbonization. Specifically, we proposed a unique architecture consisting of encapsulated CoS nanoparticles in N- and S-doped PCNFs, which can improve the ultrafast cycling performance. The CoS-NS-PCNF exhibited the highest specific surface area ($548.2 \text{ m}^2 \text{ g}^{-1}$), with a total pore volume of $0.27 \text{ cm}^3 \text{ g}^{-1}$. In addition, the novel electrode exhibited an improved Li ion diffusion coefficient ($1.72 \times 10^{-12} \text{ cm}^2 \text{ s}^{-1}$) and increased electrical conductivity ($7.9 \times 10^2 \text{ S cm}^{-1}$). The significantly improved electrochemical performance of CoS-NS-PCNF, including the high specific capacity (748.6 mAh g^{-1} with capacity retention of 96.5% at a current density of 100 mA g^{-1} after 100 cycles), superb high-rate capacity (550.4 mAh g^{-1} at a current density of 2000 mA g^{-1}), and excellent ultrafast cycling stability (514.6 mAh g^{-1} with capacity retention of 93.5% at a current density of 2000 mA g^{-1} after 500 cycles) was attributed to three main factors. First, the high specific capacity was caused by the increased number of active sites resulting from the well-dispersed CoS nanoparticles. Second, outstanding cycling stability was related to the suppression of the volume expansion by the encapsulated CoS nanoparticles in the carbon. Third, the excellent ultrafast cycling performance is attributed to the reduced Li ion diffusion length as well as the fast electron transfer rate due to the well-distributed mesopores and the doped N and S atoms in the PCNFs. The unique architectures developed in this study are promising candidates for the anode materials of ultrafast LIBs.

CRedit authorship contribution statement

Dong-Yo Shin: Conceptualization, Methodology, Investigation.
Hyun-Gi Jo: Methodology. **Hyo-Jin Ahn:** Conceptualization, Supervision, Writing - review & editing.

Declaration of Competing Interest

The authors declare that they have no known competing financial interests or personal relationships that could have appeared to influence the work reported in this paper.

Acknowledgement

This work was supported by the National Research Foundation of Korea (NRF) grant funded by the Korea government (MSIT) (No. 2019R1 A2 C1005836)

Appendix A. Supplementary data

Supplementary data to this article can be found online at <https://doi.org/10.1016/j.apsusc.2020.146895>.

References

- [1] M. Muratori, Impact of uncoordinated plug-in electric vehicle charging on residential power demand, *Nat. Energy* 3 (2018) 193–201.
- [2] C.A. Aubin, S. Choudhury, R. Jerch, L.A. Archer, J.H. Pikul, R.F. Shepherd, Electrolytic vascular systems for energy-dense robots, *Nature* 571 (2019) 51–57.
- [3] H. Lee, P. Oh, J. Kim, H. Cha, S. Chae, S. Lee, J. Cho, Advances and prospects of sulfide all-solid-state lithium batteries via one-to-one comparison with conventional liquid lithium ion batteries, *Adv. Mater.* 31 (2019) 1900376.
- [4] G.-H. An, D.-Y. Lee, H.-J. Ahn, Tunneled mesoporous carbon nanofibers with embedded ZnO nanoparticles for ultrafast lithium storage, *ACS Appl. Mater. Interface* 9 (2017) 12478–12485.
- [5] D.-Y. Shin, B.-R. Koo, H.-J. Ahn, Lithium storage kinetics of highly conductive F-doped SnO₂ interfacial layer on lithium manganese oxide surface, *Appl. Surf. Sci.* 499 (2020) 144057.
- [6] M. Ko, S. Chae, S. Jeong, P. Oh, J. Cho, Elastic a-silicon nanoparticle backboned graphene hybrid as a self-compacting anode for high-rate lithium ion batteries, *ACS Nano* 8 (2014) 8591–8599.
- [7] D. Wu, Y. Ouyang, W. Zhang, Z. Chen, Z. Li, S. Wang, F. Wang, H. Li, L.Y. Zhang, Hollow cobalt oxide nanoparticles embedded porous reduced graphene oxide anode for high performance lithium ion batteries, *Appl. Surf. Sci.* 508 (2020) 145311.
- [8] J.A. Weeks, H.-H. Sun, H.S. Srinivasan, J.N. Burrow, J.V. Guerrero, M.L. Meyerson, A. Dolocan, A. Heller, B. Mullins, Facile synthesis of a tin oxide-carbon composite lithium-ion battery anode with high capacity retention, *ACS Applied Material Interface* 2 (2019) 7244–7255.
- [9] M. Misawa, H. Hashimoto, R.K. Kalia, S. Matsumoto, A. Nakano, F. Shimojo, J. Takada, S. Tiwari, K. Tsuruta, P. Vashishta, Rapid and reversible lithiation of doped biogenous iron oxide nanoparticles, *Science Reports* 9 (2019) 1828.
- [10] J. Shao, J. Feng, H. Zhou, A. Yuan, Graphene aerogel encapsulated Fe-Co oxide nanocubes derived from Prussian blue analogue as integrated anode with enhanced Li-ion storage properties, *Appl. Surf. Sci.* 471 (2019) 745–752.
- [11] A. Jin, S.-H. Yu, J.-H. Park, S.M. Kang, M.-J. Kim, T.-Y. Jeon, J. Mun, Y.-E. Sung, Iron sulfides with dopamine-derived carbon coating as superior performance anodes for sodium-ion batteries, *Nano Res.* 12 (2019) 2609–2613.
- [12] Q. Li, L. Li, P. Wu, N. Xu, L. Wang, M. Li, A. Dai, K. Amine, L. Mai, J. Lu, Silica Restricting the sulfur volatilization of nickel sulfide for high-performance lithium-ion batteries, *Adv. Energy Mater.* 9 (2019) 1901153.
- [13] X. Wang, Y. Chen, Y. Fang, J. Zhang, S. Gao, X.W. Lou, Synthesis of cobalt sulfide multi-shelled nanoboxes with precisely controlled two to five shells for sodium-ion batteries, *Angew. Chem. Int. Ed.* 58 (2019) 2675–2679.
- [14] P. Wang, M. Shen, H. Zhou, C. Meng, A. Yuan, MOF-derived CuS@Cu-BTC composites as high-performance anodes for lithium-ion batteries, *Small* 15 (2019) 1903522.
- [15] Z. Li, W. Feng, Y. Lin, X. Liu, H. Fei, Flaky CoS₂ and graphene nanocomposite anode materials for sodium-ion batteries with improved performance, *RSC Adv.* 6 (2016) 70632–70637.
- [16] Y. Wang, J. Wu, Y. Tang, X. Lu, C. Yang, M. Qin, F. Huang, X. Li, X. Zhang, Phase-controlled synthesis of cobalt sulfides for lithium ion batteries, *ACS Appl. Mater. Interfaces* 4 (2012) 4246–4250.
- [17] H. Shangguana, W. Huang, C. Engelbrekt, X. Zheng, F. Shen, X. Xiao, L. Ci, P. Si, J. Zhang, Well-defined cobalt sulfide nanoparticles locked in 3D hollow nitrogendoped carbon shells for superior lithium and sodium storage, *Energy Storage Mater.* 7 (2017) 130–151.
- [18] J.H. Kim, J.-H. Lee, Y.C. Kang, Electrochemical properties of cobalt sulfide-carbon

- composite powders prepared by simple sulfidation process of spray dried precursor powders, *Electrochim. Acta* 137 (2014) 336–343.
- [19] M. Jin, S.-Y. Lu, L. Ma, M.-Y. Gan, Y. Lei, X.-L. Zhang, G. Fu, P.-S. Yang, M.-F. Yan, Different distribution of in-situ thin carbon layer in hollow cobalt sulfide nanocages and their application for supercapacitors, *J. Power Sources* 341 (2017) 294–301.
- [20] P. Justin, G.R. Rao, CoS spheres for high-rate electrochemical capacitive energy storage application, *Int. J. Hydrog. Energy* 35 (2010) 9709–9715.
- [21] Y. Chen, X. Li, K. Park, L. Zhou, H. Huang, Y.-W. Mai, J.B. Goodenough, Hollow nanotubes of N-doped carbon on CoS, *Angew. Chem. Int. Ed.* 55 (2016) 15831–15834.
- [22] I.M. Weiss, C. Muth, R. Drumm, H.O.K. Kirchner, Thermal decomposition of the amino acids glycine, cysteine, aspartic acid, asparagine, glutamic acid, glutamine, arginine and histidine, *BMC Biophysics* 11 (2018) 2.
- [23] K. Qu, Y. Zheng, S. Dai, S.Z. Qiao, Graphene oxide-polydopamine derived N, S-codoped carbon nanosheets as superior bifunctional electrocatalysts for oxygen reduction and evolution, *Nano Energy* 19 (2016) 373–381.
- [24] W. Si, J. Zhou, S. Zhang, S. Li, W. Xing, S. Zhuo, Tunable N-doped or dual N, S-doped activated hydrothermal carbons derived from human hair and glucose for supercapacitor applications, *Electrochim. Acta* 107 (2013) 397–405.
- [25] M. Li, C. Liu, H. Zhao, H. An, H. Cao, Y. Zhang, Z. Fan, Tuning sulfur doping in graphene for highly sensitive dopamine biosensors, *Carbon* 86 (2015) 197–206.
- [26] L. Zhang, J. Niu, M. Li, Z. Xia, Catalytic mechanisms of sulfur-doped graphene as efficient oxygen reduction reaction catalysts for fuel cells, *J. Phys. Chem. C* 118 (2014) 3545–3553.
- [27] Q. Shi, F. Peng, S. Liao, H. Wang, H. Yu, Z. Liu, B. Zhang, D. Su, Sulfur and nitrogen co-doped carbon nanotubes for enhancing electrochemical oxygen reduction activity in acidic and alkaline media, *J. Mater. Chem. A* 1 (2013) 14853.
- [28] J.H. Lee, S.H. Kwon, S. Kwon, M. Cho, K.H. Kim, T.H. Han, S.G. Lee, Tunable electronic properties of nitrogen and sulfur doped graphene: density functional theory approach, *Nanomaterials* 9 (2019) 268.
- [29] D.-Y. Shin, K.-W. Sung, H.-J. Ahn, Synergistic effect of heteroatom-doped activated carbon for ultrafast charge storage kinetics, *Appl. Surf. Sci.* 478 (2019) 499–504.
- [30] J.L. Fenton, R.E. Schaak, Structure-selective cation exchange in the synthesis of zincblende MnS and CoS nanocrystals, *Angew. Chem. Int. Ed.* 56 (2017) 6464–6467.
- [31] Q. Wang, L. Jiao, H. Du, W. Peng, Y. Han, D. Song, Y. Si, Y. Wang, H. Yuan, Novel flower-like CoS architectures: one-pot synthesis and electrochemical properties, *J. Mater. Chem.* 21 (2011) 327–329.
- [32] Z. Zhou, F. Zhang, J. Wang, X. Zhang, W. Xu, R. Wu, L. Liao, X. Wang, J. Wei, L-cysteine modified ZnO: small change while great progress, *Mater. Sci. Eng., C* 103 (2019) 109818.
- [33] J. Morales-Vidal, N. Lopez, M.A. Ortuno, Chirality transfer in gold nanoparticles by L-cysteine amino acid: a first-principles study, *J. Phys. Chem. C* 123 (2019) 13758–13764.
- [34] X. Guo, R. Wang, L. Ni, S. Qiu, Z. Zhang, Synthesis of $\text{Li}_4\text{Ti}_5\text{O}_{12}$ with tunable morphology using L-cysteine and enhanced lithium storage properties, *ChemPlusChem* 84 (2019) 123–129.
- [35] G.-H. An, H.-J. Ahn, Activated porous carbon nanofibers using Sn segregation for high-performance electrochemical capacitors, *Carbon* 65 (2013) 87–96.
- [36] G.-H. An, H. Kim, H.-J. Ahn, Improved ionic diffusion through the mesoporous carbon skin on silicon nanoparticles embedded in carbon for ultrafast lithium storage, *ACS Appl. Mater. Interfaces* 10 (2018) 6235–6244.
- [37] D.-Y. Shin, G.-H. An, H.-J. Ahn, Barnacle-like manganese oxide decorated porous carbon nanofibers for high-performance asymmetric supercapacitors, *Ceram. Int.* 44 (2018) 4883–4890.
- [38] D.-Y. Shin, D.-H. Park, H.-J. Ahn, Interface modification of an Al current collector for ultrafast lithium-ion batteries, *Appl. Surf. Sci.* 475 (2019) 519–523.
- [39] F. Han, C. Zhang, B. Sun, W. Tang, J. Yang, X. Li, Dual-carbon phase-protective cobalt sulfide nanoparticles with cable-type and mesoporous nanostructure for enhanced cycling stability in sodium and lithium ion batteries, *Carbon* 118 (2017) 731–742.
- [40] H. Wang, J. Ma, S. Liu, L. Nie, Y. Chai, X. Yang, R. Yuan, CoS/CNTs hybrid structure for improved performance lithium ion battery, *J. Alloy. Compd.* 676 (2016) 551–556.
- [41] S. Tao, W. Huang, H. Xie, J. Zhang, Z. Wang, W. Chu, B. Qian, Li Song, Formation of graphene-encapsulated CoS_2 hybrid composites with hierarchical structures for high-performance lithium-ion batteries, *RSC Adv.* 7 (2017) 39427.
- [42] Y. Yao, Y. Zhu, J. Huang, J. Shen, C. Li, Porous CoS nanosheets coated by N and S doped carbon shell on graphene foams for free-standing and flexible lithium ion battery anodes: influence of void spaces, shell and porous nanosheet, *Electrochim. Acta* 271 (2018) 242–251.
- [43] Y. Wang, Y. Zhang, Y. Peng, H. Li, J. Li, B.-J. Hwang, J. Zhao, Physical confinement and chemical adsorption of porous C/CNT micro/nano-spheres for CoS and Co_9S_8 as advanced lithium batteries anodes, *Electrochim. Acta* 299 (2019) 489–499.
- [44] F. Luo, D. Ma, Y. Li, H. Mi, P. Zhang, S. Luo, Hollow $\text{Co}_3\text{S}_4/\text{C}$ anchored on nitrogen-doped carbon nanofibers as a free-standing anode for high-performance Li-ion batteries, *Electrochim. Acta* 299 (2019) 173–181.
- [45] D. Yin, G. Huang, F. Zhang, Y. Qin, Z. Na, Y. Wu, L. Wang, Coated/sandwiched rGO/ CoS_x composites derived from metal-organic frameworks/GO as advanced anode materials for lithium-ion batteries, *Chem. Eur. J.* 22 (2016) 1467–1474.
- [46] X. Zhang, X.J. Liu, G. Wang, H. Wang, Cobalt disulfide nanoparticles/graphene/carbon nanotubes aerogels with superior performance for lithium and sodium storage, *J. Colloid Interface Sci.* 505 (2017) 23–31.
- [47] C. Xu, Y. Jing, J. He, K. Zhou, Y. Chen, Q. Li, J. Lin, W. Zhang, Self-assembled interwoven $\text{CoS}_2/\text{CNTs}/\text{graphene}$ architecture as anode for high-performance lithium ion batteries, *J. Alloy. Compd.* 708 (2017) 1178–1183.
- [48] V.G. Ahmadabadi, K. Shirvanimoghaddam, R. Kerr, N. Showkath, M. Naebe, Structure-rate performance relationship in Si nanoparticles-carbon nanofiber composite as flexible anode for lithium-ion batteries, *Electrochim. Acta* 330 (2020) 135232.
- [49] G.-H. An, D.-Y. Lee, Y.-J. Lee, H.-J. Ahn, Ultrafast Lithium Storage Using Antimony-Doped Tin Oxide Nanoparticles Sandwiched between Carbon Nanofibers and a Carbon Skin, *ACS Appl. Mater. Interfaces* 8 (2016) 30264–30270.
- [50] J. Ma, J. Sung, J. Hong, S. Chae, N. Kim, S.-H. Choi, G. Nam, Y. Son, S.Y. Kim, M. Ko, J. Cho, Towards maximized volumetric capacity via pore-coordinated design for large-volume-change lithium-ion battery anodes, *Nat. Commun.* 10 (2019) 475.